AGU PUBLICATIONS

Geophysical Research Letters

RESEARCH LETTER
10.1002/2017GL074929

Key Points:
- High-resolution surface elevation change shows channelized thinning, unabated from the grounding line up to the calving front
- Thinning is related to channelized basal melting controlled by ocean circulation and cavity geometry
- Process has been ongoing for over 25 years, thinning the shelf to 3 quarter of its original height, making it more vulnerable to collapse

Supporting Information:
- Supporting Information S1

Correspondence to:
N. Gourmelen,
noel.gourmelen@ed.ac.uk

Citation:
Gourmelen, N., Goldberg, D. N., Snow, K., Henley, S. F., Bingham, R. G., Kimura, S., … van de Berg, W. J. (2017). channelized melting drives thinning under a rapidly melting Antarctic ice shelf. *Geophysical Research Letters*, *44*, 9796–9804. https://doi.org/10.1002/2017GL074929

Received 13 JUL 2017
Accepted 27 AUG 2017
Published online 10 OCT 2017

Channelized Melting Drives Thinning Under a Rapidly Melting Antarctic Ice Shelf

Noel Gourmelen[1,2], Dan N. Goldberg[1], Kate Snow[1], Sian F. Henley[1], Robert G. Bingham[1], Satoshi Kimura[3,4,8], Anna E. Hogg[5], Andrew Shepherd[5], Jeremie Mouginot[6], Jan T. M. Lenaerts[7], Stefan R. M. Ligtenberg[7], and Willem Jan van de Berg[7]

[1]School of GeoSciences, University of Edinburgh, Edinburgh, UK, [2]IPGS UMR 7516, Université de Strasbourg, CNRS, Strasbourg, France, [3]Nansen Center and Bjerknes Centre for Climate Research, Bergen, Norway, [4]British Antarctic Survey, Cambridge, UK, [5]Center for Polar Observation and Modelling, University of Leeds, Leeds, UK, [6]Department of Earth System Science, University of California, Irvine, CA, USA, [7]Institute for Marine and Atmospheric Research Utrecht, Utrecht University, Utrecht, Netherlands, [8]Japan Agency for Marine-Earth Science and Technology, Yokosuka, Japan

Abstract Ice shelves play a vital role in regulating loss of grounded ice and in supplying freshwater to coastal seas. However, melt variability within ice shelves is poorly constrained and may be instrumental in driving ice shelf imbalance and collapse. High-resolution altimetry measurements from 2010 to 2016 show that Dotson Ice Shelf (DIS), West Antarctica, thins in response to basal melting focused along a single 5 km-wide and 60 km-long channel extending from the ice shelf's grounding zone to its calving front. If focused thinning continues at present rates, the channel will melt through, and the ice shelf collapse, within 40–50 years, almost two centuries before collapse is projected from the average thinning rate. Our findings provide evidence of basal melt-driven sub-ice shelf channel formation and its potential for accelerating the weakening of ice shelves.

Plain Language Summary Ice shelves act as safety bands around the Antarctic ice sheet. Many ice shelves are currently thinning, leading to acceleration of the grounded ice behind. Here we show that ice shelves' thinning is stronger along a channel structure formed by the ocean circulation under the ice shelf. The thinning is 3 times higher than the ice shelf's average, hence leading to a more rapid weakening of the ice shelf. This study provides evidence of basal melt-driven sub-ice shelf channel formation and its potential for accelerating the weakening of ice shelves.

1. Introduction

The majority of meteoric ice that forms in West Antarctica leaves the ice sheet through floating ice shelves, many of which have been thinning substantially over the last 25 years (Holland et al., 2015; Paolo et al., 2015; Pritchard et al., 2012; Shepherd et al., 2003). A significant proportion of ice shelf thinning has been driven by submarine melting (Depoorter et al., 2013; Rignot et al., 2013; Shepherd et al., 2003) facilitated by increased access of relatively warm (>0.6°C) (Jacobs et al., 1996; Randall-Goodwin et al., 2015; Schofield et al., 2015) modified Circumpolar Deep Water (CDW) to subshelf cavities (Dutrieux et al., 2014). Ice shelves play a significant role in stabilizing the ice sheet from runaway retreat (de Angelis & Skvarca, 2003; Pritchard et al., 2012; Rott et al., 2002; Scambos et al., 2014; Shepherd et al., 2004) and regulating its contribution to sea level change (Shepherd et al., 2012). Ice shelf melting has also been implicated in sustaining high primary productivity (PP) in Antarctica's coastal seas (Arrigo et al., 2015) (Figure 1). However, these processes vary regionally and are not fully understood. Under some ice shelves, concentrated melting leads to the formation of inverted channels (Alley et al., 2016; Berger et al., 2017; Fricker et al., 2009; Le Brocq et al., 2013; Marsh et al., 2016; Rignot & Steffen, 2008; Sergienko, 2013). These channels guide buoyant melt-laden outflow, which can lead to localized melting of the sea ice cover (Mankoff et al., 2012). In extreme cases, the ice shelf is considerably thinner along the channels, with example of channels reducing the ice shelf thickness by half (Rignot & Steffen, 2008). The channels may potentially lead to heightened crevassing, which in turn affects ice shelf stability (Vaughan et al., 2012). Meanwhile, numerical studies suggest that buttressing loss is sensitive to the location of ice removal within an ice shelf (Fürst et al., 2015; Goldberg et al., 2012). Thus, it is important that we observe spatial patterns, as well as magnitudes, of ice shelf thinning, in order to improve understanding of the ocean drivers of thinning and of their impacts on ice shelf stability.

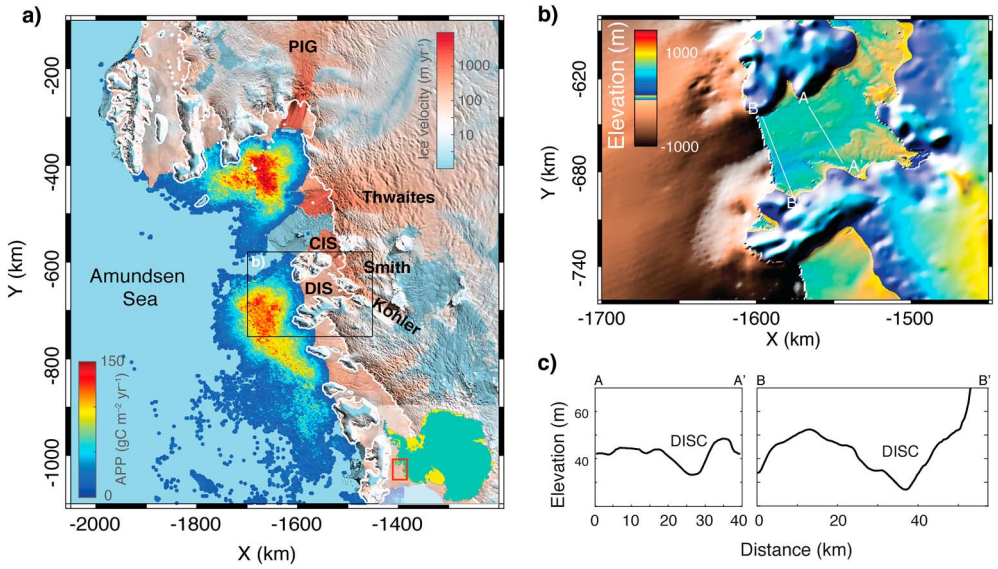

Figure 1. Dotson Ice Shelf, Amundsen Sea Sector; ice discharge, primary productivity, topography and bathymetry. (a) Ice flow of grounded ice across the grounding line (white line) feeding floating ice shelves (DIS and Crosson Ice Shelf (CIS)) and regions of high annual primary productivity (APP) (Arrigo et al., 2015). (b) Bathymetry and topography in the region of the DIS with the location of profiles (white lines) shown in Figure 1c; (c) DIS surface topography along the two profiles across DISC shown in Figure 1b—Ice flows out of page.

Dotson Ice Shelf (DIS) is a 70 km long by 50 km wide ice shelf in the Amundsen Sector of West Antarctica (Figure 1) which buttresses Kohler (KG) and Smith Glaciers (SG). In recent decades, KG and SG have exhibited significant thinning and retreat (Scheuchl et al., 2016). Between 1994 and 2012, DIS thinned at a constant rate of 2.6 m yr^{-1}, a rate 37% above the Amundsen Sea sector mean (Paolo et al., 2015), and ice discharge across the grounding line into the ice shelf increased by 180%, 30% above the Amundsen Sea sector mean (Mouginot et al., 2014). The surface ocean in front of DIS is cooled to the surface freezing point in the winter (Webber et al., 2017), and the upper ocean remains at or near the freezing point year round (Jacobs et al., 2011; Kim et al., 2017); but a deep trough traverses the continental shelf (Figure 1b), which facilitates CDW access to the subshelf cavity (Wåhlin et al., 2013), promoting high submarine melt rates. To date, only a handful of estimates of melt rates under Dotson have been made. An annually averaged submarine-melt rate of 7.8 ± 0.6 m yr^{-1} was inferred from satellite data for the period 2003–2008 (Rignot et al., 2013). At the grounding lines of KG, feeding DIS, melt rates of 40–70 m yr^{-1} have been inferred from airborne observations (Khazendar et al., 2016). Hydrographic estimates from January 2011 (Randall-Goodwin et al., 2015) suggested an ice removal rate of 81 Gt yr^{-1}—equivalent to a submarine-melt rate of ~15 m yr^{-1} using the same area baseline as the satellite estimate and an ice density of 917 kg m^{-3}. Meanwhile, a glider-based estimate from January 2014 (Miles et al., 2016) suggested ~3.5 m yr^{-1}. The latter two measurements were taken during the Austral summer, when melt rates are expected to be elevated and likely do not reflect the annual average. Importantly, none of the above results provide a detailed spatial pattern of melt and thus offer little capability for assessing the role of channels and small-scale features in defining basal melt concentration. This is important as understanding how Dotson Ice Shelf thins and is melted by the ocean is critical to predicting the future contribution to sea level of the grounded ice draining through Kohler and Smith glaciers.

2. Data and Methods

Regional-scale inferences of net melt at the ice shelf/ocean interface have relied on observations of ice shelf surface elevation change. The resolution of such net basal melting is largely constrained by the spatial resolution of the satellite altimetry measurements, which is on the order of tens of kilometers as a consequence of satellite track separations and instrument footprint size (Paolo et al., 2015; Shepherd et al., 2003) (Figure S1 in the supporting information).

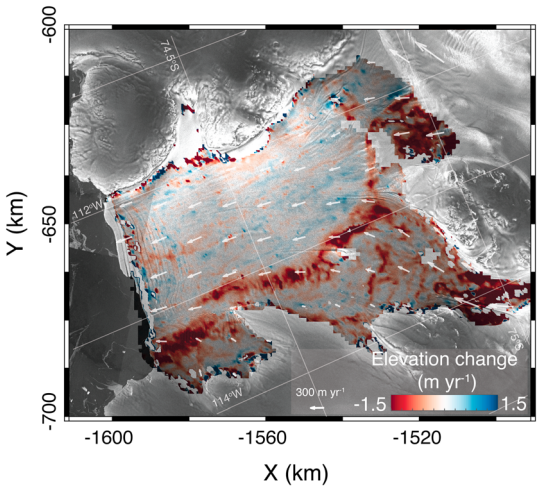

Figure 2. Rates of surface elevation change of the Dotson Ice Shelf. Lagrangian rates of surface elevation change between 2010 and 2016 from CryoSat-2 altimetry. Background shows Sentinel-1 radar images. Ice surface velocity is shown (white arrows).

In order to resolve elevation change at a spatial-scale commensurate with observed ice shelf channels, we generate a new elevation dataset using CryoSat-2 interferometric-swath radar altimetry acquired from 2010 to 2016 (Foresta et al., 2016). Swath processing leads to an order of magnitude higher spatial density than conventional radar altimetry techniques (i.e., Point-of-Closest-Approach), even over relatively flat topography found in ice shelves (Figure S1).

We then derive rates of surface elevation change $\dot{h}$ between 2010 and 2016 from the time-dependent swath elevation (Figure 2). We use a Lagrangian framework to derive $\dot{h}$ as to avoid interference of advecting ice shelf topography (Dutrieux et al., 2013; Moholdt et al., 2014). To this effect, we use ice velocity obtained from tracking of radar observation by the European Space Agency Sentinel-1a mission between 2013 and 2016 (Rignot et al., 2011; Rignot et al., 2017) (supporting information) to calculate and assign the position that each CryoSat-2 swath elevation measurements would have had at the beginning of the CryoSat-2 period, set at July 2010. The rates of surface elevation change and a Digital Elevation Model are then derived using a plane fit approach (Foresta et al., 2016) applied to the swath CryoSat-2 elevations. The map of linear rates of surface elevation change between 2010 and 2016, $\dot{h}$, and the swath Digital Elevation Model, c_2, is solved on a grid of 500 m posting. We use a simple bilinear model within each 500 m grid cell to describe the spatial variation of topography:

$$z(x, y, t) = c_0 x + c_1 y + \dot{h} t + c_2 \tag{1}$$

where z is the CryoSat-2 elevation, x, y, t are easting, northing, and time, respectively, c_0 and c_1 the topography slopes in the x and y direction, and c_2 the surface elevation at the cell center.

The chosen spatial resolution of 500 m allows observations at the length scales comparable to features associated with ice shelf melt variability of 500 m to 3 km (Alley et al., 2016; Dutrieux et al., 2013). We also quantify the change in ice velocity during the survey time period which, together with the digital elevation model (DEM), provide a measure of surface elevation change due to ice advection and ice divergence.

The melt rate of DIS is assessed through the following (Jenkins & Doake, 1991):

$$\dot{m} = \mathrm{SMB} - \left(\dot{h} + S\nabla\cdot\boldsymbol{u}\right)\cdot\frac{1}{1-\rho_{\mathrm{ice}}/\rho_{\mathrm{ocean}}} \tag{2}$$

where $\dot{m}$ is basal melt rate, SMB is the surface mass balance (van Wessem et al., 2016), ρ_{ice} is ice density of 917 kg m^{-3}, ρ_{ocean} nominal ocean density of 1,028 kg m^{-3}, $\boldsymbol{u}$ is velocity, S is surface elevation from the DEM, corrected for a 1.5 m penetration bias (Figure S3). All terms in the equation are contemporary; the ice velocity spans a slightly shorter period (2013–2016) than the other terms (2011–2016). Ice velocity differences between 2011 and 2013 are likely minimal since the Lagrangian treatment of the CryoSat elevation shows no advection residual; this suggest that the slight mismatch between ice velocity and the remainder of the balanced equation will have a negligible impact on the robustness of the calculated melt rates. A more detailed discussion of the methodology can be found in the supporting information (Arakawa & Lamb, 1977; Dehecq et al., 2015; Drews, 2016; Fretwell et al., 2013; Langley et al., 2014; Lenaerts et al., 2012; Ligtenberg et al., 2011; McMillan et al., 2011; Medley et al., 2013; Mouginot et al., 2012; Ng & King, 2011; Padman et al., 2002; Rignot et al., 2014; Timmermann et al., 2010; Trusel et al., 2013; Van Wessem et al., 2014; Zwally et al., 2012).

3. Results

The mean rate of surface elevation change for the whole of DIS between 2010 and 2016 is -0.26 ± 0.03 m yr^{-1}, which is consistent within errors with the rate of -0.28 ± 0.03 m yr^{-1} reported for 1994–2012 (Paolo et al., 2015). Strikingly, however, the finer resolution of our measurements enables us to discriminate parts of the DIS where the absolute rates are significantly larger, locally exceeding 1 m yr^{-1}. A feature, visible along the

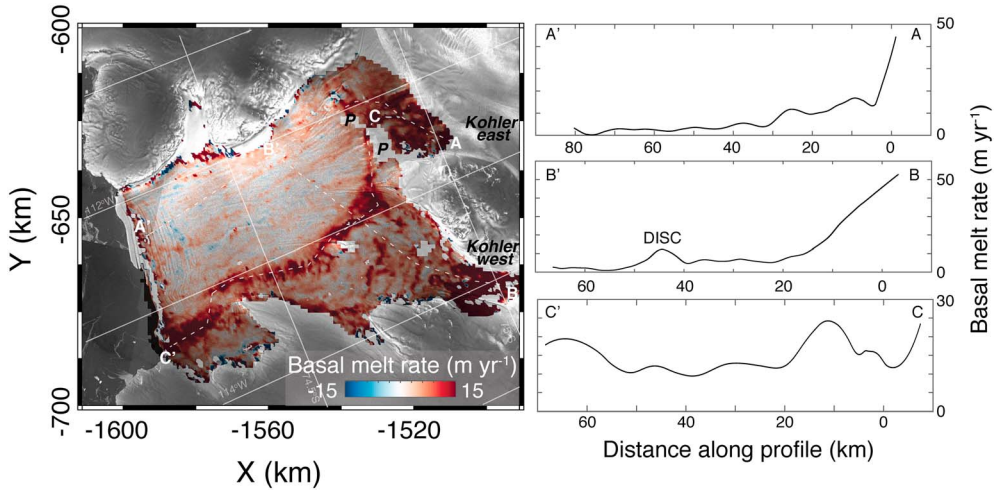

Figure 3. Total basal melt rates of the Dotson Ice Shelf. (left) Spatial distribution of basal melt rates, location of profiles indicated by dashed curves. The profiles show melt rates across the ice shelf from the Kohler east grounding line (A-A′) and Kohler west grounding line (B-B′), and along the DISC (C-C′). Location of pinning points (P) identified in text and Kohler east and Kohler west glaciers.

western edge of the DIS, consists of a quasi-continuous ~5 km-wide band of negative elevation change extending from the southern (landward) sector of the ice shelf to the ice shelf calving front (Figure 2). Along this feature, henceforth termed the DIS Channel (DISC), the mean rate of elevation change is -0.76 ± 0.03 m yr^{-1}, which accounts for 30% of the total elevation change of DIS.

Along the DISC, ice is significantly thinner than found elsewhere across the ice shelf, with surface elevation 10 to 20 m below the surrounding areas. The surface elevation depression is matched by a subshelf channel incised upward into the ice to between 100 and 200 m (supporting information S2). While much of the recent thinning of DIS has clearly been concentrated along the DISC, it is unknown for how long this process has formed a major component of the ice shelf's loss. From ice velocity measurements acquired in 2008, the DISC can be discerned as a region of broad ice convergence, suggesting that focused basal melting was already occurring there by 2008 (Rignot et al., 2013). Surface elevation change between 1991 and 2010, computed from lower spatial resolution radar altimetry (Figure S5), shows that the broad region around the DISC was lowering at rates of 0.5 m yr^{-1}, significantly faster than the remainder of DIS that was lowering at $<$0.1 m yr^{-1}. These indirect and sparse observations suggest that the localized thinning observed between 2010 and 2016 has been ongoing for at least two decades.

To elucidate the potential causes of the concentrated ice shelf thinning observed along the DISC, we considered various factors. A comparison of DIS's velocity structure in 2015 with that of 2008 (Figure S9) shows that changes in ice divergence could not be the cause of the observed signal in the altimetry data and hence that the observed surface lowering does not have an ice-dynamic origin. We also eliminate any explanation that invokes surface processes, because the magnitudes of changes related to surface processes are small here (Figure S8) and no evidence of surface melt has been recorded (Kingslake et al., 2017). We propose that the most likely explanation for the observed surface lowering is thinning caused by melting at the base of the ice shelf.

We find that basal melt is concentrated at the grounding line of KG east and KG west and along the DISC and that little melt occurs elsewhere under DIS (Figure 3). The total $\dot{m}$ under DIS amounts to an average basal melt of 6.1 ± 0.7 m yr^{-1}. The basal melting under the Kohler east and Kohler west grounding lines dominates the total basal melt budget, with rates of up to 50 m yr^{-1} (Figure 3), in agreement with values of 40 to 70 m yr^{-1} derived from local airborne surveys (Khazendar et al., 2016). Elsewhere in DIS, basal melt is concentrated along the DISC, averaging 14 m yr^{-1} (Figure 3). The channelized melt pattern is continuous, from the grounding zone of Kohler east to DIS's calving front. We observe continuous melt across a series of pinning points between Kohler east and DIS, indicating that this region of the DIS, near Kohler

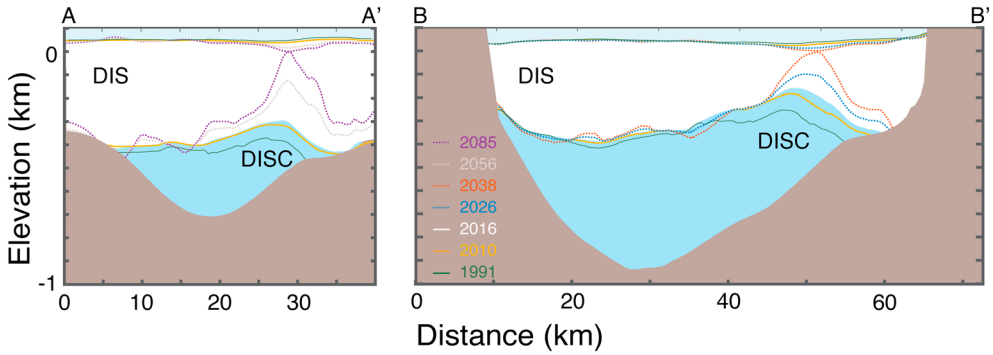

Figure 4. Observed and projected thickness evolution of the Dotson Ice Shelf. Between 2010 and 2016 DIS has lost an average of 7 m of ice along the DISC with very little thinning elsewhere with the exception of the KG grounding line. Elevation change from lower resolution observations between 1991 and 2010 (green solid line) show that thinning at DISC has been taking place over the last 25 years. Colored dashed lines are a simple projection of ice thickness across the channel (see Figure 1c for location) if current thinning rates were to persist.

east, is ungrounded at the time of our observations, supporting observation of ongoing grounding line retreat (Scheuchl et al., 2016).

4. Discussion

A large number of channels observed around Antarctica are thought to be driven by subglacial runoff (Drews et al., 2017; Le Brocq et al., 2013). However, the size of runoff-driven melt channels generated at the grounding lines is known to diminish with the distance from the grounding line (Drews, 2016; Dutrieux et al., 2014; Le Brocq et al., 2013). This is counter to our observations along the DISC showing sustained melt rate and thinning along the entire length of the channel (Figure 3). We therefore suggest that DISC is mainly the result of ocean forcing rather than related to subglacial or grounding line processes. This is in agreement with Alley et al. (2016), who classify the majority of sub-ice shelf channels in the Amundsen and Bellingshausen (including DISC) as "ocean sourced," as opposed to being driven by subglacial runoff (subglacially sourced). The authors attribute this to the extensive CDW on the continental shelf. It is generally thought that CDW enters DIS cavity by way of a trough at the ice shelf front (Wåhlin et al., 2013), though new estimates of bathymetry suggest a connection with Crosson Ice Shelf in the southeast corner of Dotson, near the Kohler East grounding line (Millan et al., 2017). Thus, it is conceivable that some of the forcing originates from the east, in Pine Island Bay.

Regardless of the CDW source, the location of the meltwater outflow is a straightforward consequence of ocean physics: warm water, originating at depth and becoming buoyant due to melt freshening, flows along the ice shelf bottom and is guided to the left by Coriolis forces. Ocean circulation and ice thinning then self-organize to yield the thinning pattern observed. Evidence of this process is given by the observation of elevated melt on the Coriolis-favored side of DISC (Figure S7) supporting the hypothesis that water flowing within DISC is deflected by Coriolis and thus is guided by the channel itself. This conceptual method of channel formation is distinct from that of subglacially sourced channels such as that observed in Roi Baudoin ice shelf (Drews et al., 2017), as the buoyant driver required for the high velocities that lead to amplified melt (Jenkins, 2011) comes from the melt itself, not the fresh subglacial runoff. This may be why the melt (and hence the channel) can persist to the ice shelf front, rather than diminishing with distance from the grounding line, and suggests that the presence of CDW is prerequisite for the DISC to exist.

We point out that to show conclusively that the location of DISC is a result of such self-organization would require sophisticated coupled ice-ocean modeling of DIS and its cavity. Modeling studies which have investigated coupled ice-ocean dynamics of idealized ice shelves forced by warm waters (Goldberg et al., 2012; Sergienko, 2013) have spontaneously yielded marginal melt-driven channels in absence of subglacial runoff, suggesting self-organization can occur.

Upon examination of transverse surface and basal profiles (Figures 1c, 4, and supporting information section S2), most profiles exhibit the asymmetry demonstrated by Alley et al. (2016) with the apex of melting

occurring on the Coriolis-favored side of the channel (Figure S7), which is thought to be caused by geostrophic "slumping" of the fast-flowing water to the Coriolis-favored side. The observed asymmetry is variable along the channel which is consistent with an ocean-sourced mechanism, a number of factors (e.g., water velocity, mixed layer depth, and steepness of the ice shelf base in the flow direction) govern the relative importance of the Coriolis force. Moreover, suggestion that asymmetry might be less strong where melting is higher (Dutrieux et al., 2013) could also explain the variability in observed asymmetry along the channel.

Our observations have implications for the stability of DIS. A simple forward projection using the currently observed pattern and rates of thinning leads to complete melt through of the DISC within 40 years (Figure 4); 170 years earlier than DIS would thin to zero using the ice shelf averaged thinning rate although considerable uncertainties are attached to this projection. While the forward projection of current rates of thinning implicitly takes into account current melting, advection, and dynamic thinning rates, it discounts the possibility that they will likely change as the ice thins, and it is known that a moderate acceleration of DIS flow is ongoing (McMillan et al., 2012; Mouginot et al., 2014). In this respect, the location of amplified thinning may be critical. Recent studies have shown that the stability of many ice shelves, as well as the response of grounded ice, is critically sensitive to buttressing at the shear margins (Borstad et al., 2013; Fürst et al., 2016; Goldberg et al., 2012), which can be limited by marginal thinning. Moreover, while deeply incised channels have been observed to nearly melt through ice shelves (Rignot & Steffen, 2008), additional processes could be taking place as DISC continues to thin and before it reaches complete melt through; amplified thinning along shear margins will lead to increased rates of crevassing, further weakening the buttressing ability of DIS and accelerating the potential for ice shelf collapse (Alley et al., 2016; Khazendar et al., 2007, 2011).

The extent to which the present thinning will sustain is also uncertain as the timing of the ocean perturbation that has led to the current imbalance is unknown. As indicated above, DIS has likely been melting out of balance for two decades or more. Numerical experiments suggest that an ice shelf exposed to persistent melt reaches an equilibrium on a time scale commensurate with the ice shelf residence time; i.e., the average time it takes for a column of ice to traverse the shelf (Goldberg et al., 2012; Little et al., 2012; Seroussi et al., 2017). For DIS this time scale is 50–100 years, suggesting that the high melt rates observed now originated in the twentieth century.

The prominence of localized, along-channel ice shelf thinning in the high-resolution satellite altimetry record across DIS has allowed us here to explore ocean-driven sub-ice shelf melting processes. Ice shelf thinning due to channelized ocean-sourced melting has seldom been observed across Antarctic ice shelves, likely not because the process is absent, but because the resolution of observations and complexities such as advection of complex topography makes it more difficult to identify. The increasing availability of high spatial resolution altimetry and of ice velocity observation at sufficient temporal resolution will greatly help the global identification of basal channelization under ice shelves. Episodic polynya formation at the fronts of other key ice shelves, such as at Pine Island Glacier (Mankoff et al., 2012), testifies to the existence of large subshelf channels elsewhere. Moreover, the ice shelf characteristics most key to the occurrence of ocean-driven channelized melting—exposure to intrusion of warm CDW and position in a semiclosed embayment—are common for a number of Antarctic ice shelves. It is therefore likely that the pattern and importance of melt-driven thinning along boundaries or shear margins of ice shelves we have identified here is widespread and is currently weakening ice shelves elsewhere around Antarctica.

5. Conclusions

We demonstrate that swath processing of CryoSat-2 data can lead to 1 order of magnitude increase in elevation measurement over ice shelves, providing the possibility to derive a unique set of global and detailed observations of time-dependent melt rates along ice shelves' channels. Using these high-resolution measurements of time-dependent elevation change, we show that channelized thinning has been taking place at the Dotson Ice Shelf between the years 2010 and 2016 and that out-of-balance thinning has likely been sustained for the last 25 years. Unlike observations at other ice shelves, we find here that channelized thinning is sustained from the grounding line up to the ice shelf's calving front and is caused by elevated basal melting located on the Coriolis-favored side of the channel forced by ocean circulation within the subshelf cavity. The subshelf channel incises 100 to 200 m into the shelf and exceeds in place the thickness of the ice

above; if current thinning rates persist, the channel would melt through by the end of the century. It is however likely that the ice shelf will respond to the imbalance before this occurs, potentially leading to an extension of the region of thinning, increased calving or potential collapse although the nature of this response is uncertain. Whatever the type of response, continued thinning and or collapse of DIS, it will lead to increase discharge of the grounded ice draining into the Dotson and Crosson ice shelves.

Acknowledgments
This work was supported by European Space Agency contracts CryoTop 4000107394/12/I-NB and CryoTop evolution 4000116874/16/I-NB (NG), a NERC grant NE/M003590/1 (D. G.), a NERC Independent Research Fellowship NE/K010034/1 (S. H.), an independent research fellowship 4000112797/15/I-SBo (A. H.) jointly funded by the European Space Agency, the University of Leeds and the British Antarctic Survey. We thank K. Arrigo, K. Lowry, and P. Jager for providing primary productivity data across the Amundsen Sea Sector. The CryoSat-2 satellite altimetry data are freely available from the European Space Agency (https://earth.esa.int/web/guest/data-access), and the specific data used in this study are provided within the supporting information. The IceBridge airborne altimetry data are freely available from the National Snow and Ice Data Centre (https://nsidc.org/data/icebridge/). The ice velocity data are freely available from the National Snow and Ice Data Centre (https://nsidc.org/data/nsidc-0484/). We are grateful to Reinhard Drews and an anonymous reviewer and the Editor, whose comments have significantly improved the manuscript.

References

Arakawa, A., & Lamb, V. R. (1977). Computational design of the basic dynamical processes of the UCLA general circulation model. In J. Chang (Ed.), *Methods in Computational Physics: Advances in Research and Applications* (Vol. 17, pp. 173–265). New York, Elsevier.

Alley, K. E., Scambos, T. A., Siegfried, M. R., & Fricker, H. A. (2016). Impacts of warm water on Antarctic ice shelf stability through basal channel formation. *Nature Geoscience*, *9*, 290–293.

Arrigo, K. R., van Dijken, G. L., & Strong, A. L. (2015). Environmental controls of marine productivity hot spots around Antarctica. *Journal of Geophysical Research: Oceans*, *120*, 5545–5565.

Berger, S., Drews, R., Helm, V., Sun, S., & Pattyn, F. (2017). Detecting high spatial variability of ice-shelf basal mass balance (Roi Baudouin ice shelf, Antarctica). *The Cryosphere Discussions*, *2017*, 1–22.

Borstad, C. P., Rignot, E., Mouginot, J., & Schodlok, M. P. (2013). Creep deformation and buttressing capacity of damaged ice shelves: Theory and application to Larsen C ice shelf. *The Cryosphere*, *7*, 1931–1947.

de Angelis, H., & Skvarca, P. (2003). Glacier surge after ice shelf collapse. *Science*, *299*, 1560–1562.

Dehecq, A., Gourmelen, N., & Trouve, E. (2015). Deriving large-scale glacier velocities from a complete satellite archive: Application to the Pamir–Karakoram–Himalaya, Remote Sens. *Environment*, *162*, 55–66.

Depoorter, M. A., Bamber, J. L., Griggs, J. A., Lenaerts, J. T. M., Ligtenberg, S. R. M., van den Broeke, M. R., & Moholdt, G. (2013). Calving fluxes and basal melt rates of Antarctic ice shelves. *Nature*, *502*, 89–92.

Drews, R. (2016). Evolution of ice-shelf channels in Antarctic ice shelves. *The Cryosphere*, *9*, 1169–1181.

Drews, R., Brown, J., Matsuoka, K., Witrant, E., Philippe, M., Hubbard, B., & Pattyn, F. (2016). Constraining variable density of ice shelves using wide-angle radar measurements. *The Cryosphere*, *10*, 811–823.

Drews, R., Pattyn, F., Hewitt, I. J., Ng, F. S. L., Berger, S., Matsuoka, K., … Neckel, N. (2017). Actively evolving subglacial conduits and eskers initiate ice shelf channels at an Antarctic grounding line. *Nature Communications*, *8*, 15,228.

Dutrieux, P., Vaughan, D. G., Corr, H. F. J., Jenkins, A., Holland, P. R., Joughin, I., & Fleming, A. H. (2013). Pine Island glacier ice shelf melt distributed at kilometre scales. *The Cryosphere*, *7*, 1543–1555.

Dutrieux, P., De Rydt, J., Jenkins, A., Holland, P. R., Ha, H. K., Lee, S. H., … Schröder, M. (2014). Strong sensitivity of Pine Island ice-shelf melting to climatic variability. *Science*, *343*, 174–178.

Foresta, L., Gourmelen, N., Pálsson, F., Nienow, P., Björnsson, H., & Shepherd, A. (2016). Surface elevation change and mass balance of Icelandic ice caps derived from swath mode CryoSat-2 altimetry. *Geophysical Research Letters*, *43*, 12,138–12,145. https://doi.org/10.1002/2016GL071485

Fretwell, P., Pritchard, H. D., Vaughan, D. G., Bamber, J. L., Barrand, N. E., Bell, R., … Zirizzotti, A. (2013). Bedmap2: Improved ice bed, surface and thickness datasets for Antarctica. *The Cryosphere*, *7*, 375–393.

Fricker, H. A., Coleman, R., Padman, L., Scambos, T. A., Bohlander, J., & Brunt, K. M. (2009). Mapping the grounding zone of the Amery Ice Shelf, East Antarctica using InSAR, MODIS and ICESat. *Antarctic Science*, *21*, 515–532.

Fürst, J. J., Durand, G., Gillet-Chaulet, F., Merino, N., Tavard, L., Mouginot, J., … Gagliardini, O. (2015). Assimilation of Antarctic velocity observations provides evidence for uncharted pinning points. *The Cryosphere*, *9*, 1427–1443.

Fürst, J. J., Durand, G., Gillet-Chaulet, F., Tavard, L., Rankl, M., Braun, M., & Gagliardini, O. (2016). The safety band of Antarctic ice shelves. *Nature Climate Change*, *6*, 479–482.

Goldberg, D. N., Little, C. M., Sergienko, O. V., Gnanadesikan, A., Hallberg, R., & Oppenheimer, M. (2012). Investigation of land ice-ocean interaction with a fully coupled ice-ocean model: 2. Sensitivity to external forcings. *Journal of Geophysical Research*, *117*, F02038. https://doi.org/10.1029/2011JF002247

Holland, P. R., Brisbourne, A., Corr, H. F. J., McGrath, D., Purdon, K., Paden, J., … Fleming, A. H. (2015). Oceanic and atmospheric forcing of Larsen C Ice-Shelf thinning. *The Cryosphere*, *9*, 1005–1024.

Jacobs, S. S., Hellmer, H. H., & Jenkins, A. (1996). Antarctic ice sheet melting in the Southeast Pacific. *Geophysical Research Letters*, *23*, 957–960.

Jacobs, S. S., Jenkins, A., Giulivi, C. F., & Dutrieux, P. (2011). Stronger ocean circulation and increased melting under Pine Island Glacier ice shelf. *Nature Geoscience*, *4*, 519–523.

Jenkins, A., & Doake, C. S. M. (1991). Ice-ocean interaction on Ronne Ice Shelf, Antarctica. *Journal of Geophysical Research*, *96*, 791–813.

Jenkins, A. (2011). Convection-driven melting near the grounding lines of ice shelves and tidewater glaciers. *Journal of Physical Oceanography*, *41*, 2279–2294.

Khazendar, A., Rignot, E., & Larour, E. (2007). Larsen B Ice Shelf rheology preceding its disintegration inferred by a control method. *Geophysical Research Letters*, *34*, L19503. https://doi.org/10.1029/2007GL030980

Khazendar, A., Rignot, E., & Larour, E. (2011). Acceleration and spatial rheology of Larsen C Ice Shelf, Antarctic Peninsula. *Geophysical Research Letters*, *38*, L09502. https://doi.org/10.1029/2011GL046775

Khazendar, A., Rignot, E., Schroeder, D. M., Seroussi, H., Schodlok, M. P., Scheuchl, B., … Velicogna, I. (2016). Rapid submarine ice melting in the grounding zones of ice shelves in West Antarctica. *Nature Communications*, *7*, 13,243.

Kim, T. W., Ha, H. K., Wåhlin, A. K., Lee, S. H., Kim, C. S., Lee, J. H., & Cho, Y. K. (2017). Is Ekman pumping responsible for the seasonal variation of warm circumpolar deep water in the Amundsen Sea? *Continental Shelf Research*, *132*, 38–48.

Kingslake, J., Ely, J. C., Das, I., & Bell, R. E. (2017). Widespread movement of meltwater onto and across Antarctic ice shelves. *Nature*, *544*, 349–352.

Langley, K., von Deschwanden, A., Kohler, J., Sinisalo, A., Matsuoka, K., Hattermann, T., … Isaksson, E. (2014). Complex network of channels beneath an Antarctic ice shelf. *Geophysical Research Letters*, *41*, 1209–1215. https://doi.org/10.1002/2013GL058947

Lenaerts, J. T. M., van den Broeke, M. R., van de Berg, W. J., van Meijgaard, E., & Kuipers Munneke, P. (2012). A new, high-resolution surface mass balance map of Antarctica (1979–2010) based on regional atmospheric climate modeling. *Geophysical Research Letters*, *39*, L04501. https://doi.org/10.1029/2011GL050713

Le Brocq, A. M., Ross, N., Griggs, J. A., Bingham, R. G., Corr, H. F. J., Ferraccioli, F., … Siegert, M. J. (2013). Evidence from ice shelves for channelized meltwater flow beneath the Antarctic Ice Sheet. *Nature Geoscience*, *6*, 945–948.
Ligtenberg, S. R. M., Helsen, M. M., & van den Broeke, M. R. (2011). An improved semi-empirical model for the densification of Antarctic firn. *The Cryosphere*, *5*, 809–819.
Little, C. M., Goldberg, D., Gnanadesikan, A., & Oppenheimer, M. (2012). On the coupled response to ice-shelf basal melting. *Journal of Glaciology*, *58*, 203–215.
Mankoff, K. D., Jacobs, S. S., Tulaczyk, S. M., & Stammerjohn, S. E. (2012). The role of Pine Island Glacier ice shelf basal channels in deep-water upwelling, polynyas and ocean circulation in Pine Island Bay. *Antarctic*, *53*, 23–28.
Marsh, O. J., Fricker, H. A., Siegfried, M. R., Christianson, K., Nicholls, K. W., Corr, H. F. J., & Catania, G. (2016). High basal melting forming a channel at the grounding line of Ross Ice Shelf, Antarctica. *Geophysical Research Letters*, *43*, 250–255. https://doi.org/10.1002/2015GL066612
McMillan, M., Shepherd, A., Nienow, P., & Leeson, A. (2011). Tide model accuracy in the Amundsen Sea, Antarctica, from radar interferometry observations of ice shelf motion. *Journal of Geophysical Research*, *116*, C11008. https://doi.org/10.1029/2011JC007294
McMillan, M., Shepherd, A., Gourmelen, N., Park, J. W., Nienow, P., Rinne, E., & Leeson, A. (2012). Mapping ice-shelf flow with interferometric synthetic aperture radar stacking. *Journal of Glaciology*, *58*, 265–277.
Medley, B., Joughin, I., Das, S. B., Steig, E. J., Conway, H., Gogineni, S., … Nicolas, J. P. (2013). Airborne-radar and ice-core observations of annual snow accumulation over Thwaites Glacier, West Antarctica confirm the spatiotemporal variability of global and regional atmospheric models. *Geophysical Research Letters*, *40*, 3649–3654. https://doi.org/10.1002/grl.50706
Miles, T., Lee, S. H., Wåhlin, A., Ha, H. K., Kim, T. W., Assmann, K. M., & Schofield, O. (2016). Glider observations of the Dotson Ice Shelf outflow. *Deep Sea Research Part II: Topical Studies in Oceanography*, *123*, 16–29.
Millan, R., Rignot, E., Bernier, V., Morlighem, M., & Dutrieux, P. (2017). Bathymetry of the Amundsen Sea Embayment sector of West Antarctica from Operation IceBridge gravity and other data. *Geophysical Research Letters*, *44*, 1360–1368. https://doi.org/10.1002/2016GL072071
Moholdt, G., Padman, L., & Fricker, H. A. (2014). Basal mass budget of Ross and Filchner-Ronne ice shelves, Antarctica, derived from Lagrangian analysis of ICESat altimetry. *Journal of Geophysical Research: Earth Surface*, *119*, 2361–2380. https://doi.org/10.1002/2016GL072071
Mouginot, J., Scheuchl, B., & Rignot, E. (2012). Mapping of ice motion in Antarctica using synthetic-aperture radar data. *Remote Sensing*, *4*, 2,753.
Mouginot, J., Rignot, E., & Scheuchl, B. (2014). Sustained increase in ice discharge from the Amundsen Sea Embayment, West Antarctica, from 1973 to 2013. *Geophysical Research Letters*, *41*, 1576–1584. https://doi.org/10.1002/2013GL059069
Ng, F., & King, E. C. (2011). Kinematic waves in polar firn stratigraphy. *Journal of Glaciology*, *57*, 1119–1134.
Padman, L., Fricker, H. A., Coleman, R., Howard, S., & Erofeeva, L. (2002). A new tide model for the Antarctic ice shelves and seas. *Annals of Glaciology*, *34*, 247–254.
Paolo, F. S., Fricker, H. A., & Padman, L. (2015). Volume loss from Antarctic ice shelves is accelerating. *Science*, *348*, 327–331.
Pritchard, H. D., Ligtenberg, S. R. M., Fricker, H. A., Vaughan, D. G., Van den Broeke, M. R., & Padman, L. (2012). Antarctic ice-sheet loss driven by basal melting of ice shelves. *Nature*, *484*, 502–505.
Randall-Goodwin, E., Meredith, M. P., Jenkins, A., Yager, P. L., Sherrell, R. M., Abrahamsen, E. P., … Stammerjohn, S. E. (2015). Freshwater distributions and water mass structure in the Amundsen Sea Polynya region, Antarctica. *Elementa: Science of the Anthropocene*, *3*, 65.
Rignot, E., & Steffen, K. (2008). Channelized bottom melting and stability of floating ice shelves. *Geophysical Research Letters*, *35*, L02503.
Rignot, E., Mouginot, J., & Scheuchl, B. (2011). Ice flow of the Antarctic ice sheet. *Science*, *333*, 1427–1430.
Rignot, E., Jacobs, S., Mouginot, J., & Scheuchl, B. (2013). Ice-shelf melting around Antarctica. *Science*, *341*, 266–270.
Rignot, E., Mouginot, J., Morlighem, M., Seroussi, H., & Scheuchl, B. (2014). Widespread, rapid grounding line retreat of Pine Island, Thwaites, Smith, and Kohler glaciers, West Antarctica, from 1992 to 2011. *Geophysical Research Letters*, *41*, 3502–3509. https://doi.org/10.1002/2014GL060140
Rignot, E., Mouginot, J., & Scheuchl, B. (2017). MEaSUREs InSAR-based Antarctica ice velocity map, Version 2. Boulder, Colorado USA. NASA National Snow and Ice Data Center Distributed Active Archive Center. https://doi.org/10.5067/D7GK8F5J8M8R, NASA National Snow and Ice Data Center Distributed Active Archive Center.
Rott, H., Rack, W., Skvarca, P., & de Angelis, H. (2002). Northern Larsen ice shelf, Antarctica: Further retreat after collapse. *Annals of Glaciology*, *34*, 277.
Scambos, T. A., Berthier, E., Haran, T., Shuman, C. A., Cook, A. J., Ligtenberg, S. R. M., & Bohlander, J. (2014). Detailed ice loss pattern in the northern Antarctic Peninsula: Widespread decline driven by ice front retreats. *The Cryosphere*, *8*, 2135–2145.
Scheuchl, B., Mouginot, J., Rignot, E., Morlighem, M., & Khazendar, A. (2016). Grounding line retreat of Pope, Smith, and Kohler Glaciers, West Antarctica, measured with Sentinel-1a radar interferometry data. *Geophysical Research Letters*, *43*, 8572–8579. https://doi.org/10.1002/2016GL069287
Schofield, O., Miles, T., Alderkamp, A., Lee, S., Haskins, C., Rogalsky, E., … Yager, P. L. (2015). *In situ phytoplankton distributions in the Amundsen Sea Polynya measured by autonomous gliders*. Elementa: Science of the Anthropocene.
Sergienko, O. V. (2013). Basal channels on ice shelves. *Journal of Geophysical Research: Earth Surface*, *118*, 1342–1355. https://doi.org/10.1002/jgrf.20105
Seroussi, H., Nakayama, Y., Larour, E., Menemenlis, D., Morlighem, M., Rignot, E., & Khazendar, A. (2017). Continued retreat of Thwaites Glacier, West Antarctica, controlled by bed topography and ocean circulation. *Geophysical Research Letters*, *44*, 6191–6199. https://doi.org/10.1002/2017GL072910
Shepherd, A., Wingham, D., Payne, T., & Skvarca, P. (2003). Larsen ice shelf has progressively thinned. *Science*, *302*, 856–859.
Shepherd, A., Wingham, D., & Rignot, E. (2004). Warm ocean is eroding West Antarctic Ice Sheet. *Geophysical Research Letters*, *31*, L23402 DOI: https://doi.org/10.1029/2004GL021106
Shepherd, A., Ivins, E. R., Geruo, A., Barletta, V. R., Bentley, M. J., Bettadpur, S., … Jay Zwally, H. (2012). A reconciled estimate of ice-sheet mass balance. *Science*, *338*, 1183–1189.
Timmermann, R., Le Brocq, A., Deen, T., Domack, E., Dutrieux, P., Galton-Fenzi, B., … Smith, W. H. F. (2010). Antarctic ice sheet topography, cavity geometry, and global bathymetry (RTopo 1.0.5-beta), Supplement to: Timmermann, R. et al. (2010): A consistent dataset of Antarctic ice sheet topography, cavity geometry, and global bathymetry. *Earth System Science Data*, *2*(2), 261–273. https://doi.org/10.5194/essd-2-261-2010
Trusel, L. D., Frey, K. E., Das, S. B., Munneke, P. K., & van den Broeke, M. R. (2013). Satellite-based estimates of Antarctic surface meltwater fluxes. *Geophysical Research Letters*, *40*, 6148–6153. https://doi.org/10.1002/2013GL058138
Van Wessem, J. M., Reijmer, C. H., Morlighem, M., Mouginot, J., Rignot, E., Medley, B., … Van Meijgaard, E. (2014). Improved representation of East Antarctic surface mass balance in a regional atmospheric climate model. *Journal of Glaciology*, *60*, 761–770.

van Wessem, J. M., Ligtenberg, S. R. M., Reijmer, C. H., van de Berg, W. J., van den Broeke, M. R., Barrand, N. E., … van Meijgaard, E. (2016). The modelled surface mass balance of the Antarctic Peninsula at 5.5 km horizontal resolution. *The Cryosphere*, *10*, 271–285.

Vaughan, D. G., Corr, H. F. J., Bindschadler, R. A., Dutrieux, P., Gudmundsson, G. H., Jenkins, A., … Wingham, D. J. (2012). Subglacial melt channels and fracture in the floating part of Pine Island Glacier, Antarctica. *Journal of Geophysical Research*, *117*, F03012. https://doi.org/10.1029/2012JF002360

Wåhlin, A. K., Kalén, O., Arneborg, L., Björk, G., Carvajal, G. K., Ha, H. K., … Stranne, C. (2013). Variability of warm deep water inflow in a submarine trough on the Amundsen Sea shelf. *Journal of Physical Oceanography*, *43*, 2054–2070.

Webber, B. G. M., Heywood, K. J., Stevens, D. P., Dutrieux, P., Abrahamsen, E. P., Jenkins, A., … Kim, T. W. (2017). Mechanisms driving variability in the ocean forcing of Pine Island Glacier. *Nature Communications*, *8*, 14,507.

Zwally, H. J., Giovinetto, M. B., Beckley, M. A., & Saba, J. L. (2012). Antarctic and Greenland Drainage Systems, GSFC Cryospheric Sciences Laboratory.

Supplementary material to:

CHANNELIZED MELTING DRIVES THINNING UNDER A RAPIDLY MELTING ANTARCTIC ICE SHELF

S1. ELEVATION AND RATES OF ELEVATION CHANGE

CryoSat-2 Elevation

We derive surface elevation using swath processing of CryoSat-2 SARIn mode data [*Hawley et al.,* 2009; *Gray et al.,* 2013; *Foresta et al.,* 2016]. We apply swath processing to CryoSat-2 data as it provides improved spatial coverage over conventional Point-Of-Closest-Approach (POCA) altimetry [*Foresta et al.,* 2016] (Figure S1). Swath processing uses CryoSat-2 (CS2) L1b baseline C SARIn data from the European Space Agency (ESA) as input. After filtering the waveform to reject samples with low coherence (<0.8) and unwrapping on a per-waveform basis [*Gray et al.,* 2013], we correct the range for fluctuations in dry and wet tropospheric mass, the effect of the ionosphere, inverse barometric atmospheric pressure variations, and the solid Earth and ocean loading tides. The ocean tide amplitude is simulated and removed from the CryoSat-2 range measurement using the CATS2008 ocean tide model, which is an updated version of the data assimilation model [*Padman et al.,* 2002]. We use the CATS2008 ocean tide correction rather than the FES2004 ocean tide correction provided with CryoSat-2 because the spatial extent of the CATS2008 model domain provides a better match to the known ocean - land boundary in Antarctica, and the phase and amplitude of the CATS2008 tide model is more accurate than other tide model simulations in coastal Antarctica [*McMillan et al.,* 2011]. We then convert the range, across-track look angle, platform attitude and orbit parameters of all echoes into a swath of elevations relative to a reference ellipsoid. The resulting elevation dataset can be affected by phase ambiguity errors in regions with terrain slope such as at the boundary between floating and grounded ice. We solve for phase ambiguity by applying, on a waveform by waveform basis, the 2π multiple that minimizes elevation differences with respect to Bedmap2 reference Digital Elevation Model (DEM) [*Fretwell et al.,* 2013]. An error of a 2π multiple leads to errors in the mean elevation, terrain

slope and geographic location of the CryoSat-2 measurements of elevation, all leading to departure of over a 100 m from the true elevation; for these reasons, the accuracy of the Bedmap2 DEM is well within the range needed to solve for the correct phase ambiguity. We also discard elevations that differ more than 100 m w.r.t. the DEM, such high discrepancies may not be attributed to real surface elevation or elevation change and result from poor radar echoes; these represent less than 3% of the total number of measurements.

The standard elevation product from radar altimetry relies on waveform retracking to derive the elevation at the Point-Of-Closest-Approach (POCA) – leading to one measure of elevation per waveform. POCA elevations are from the ESA archive (L2, baseline C product) found at ftp://science-pds.CryoSat-2.esa.int (accessed on 06/2016).

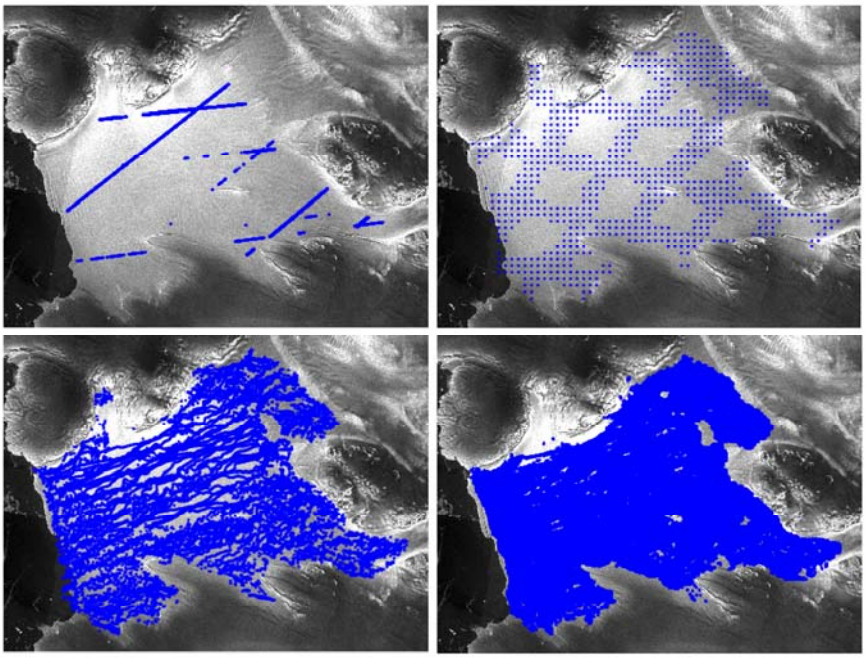

Figure S1: Spatial coverage of surface elevation over Dotson Ice Shelf from successive altimetry mission: IceSat (top-left), ERS1/2 and Envisat (top right), CryoSat-2 POCA (bottom left) and CryoSat-2 swath (bottom right). Swath processing generate over one of order of magnitude more elevation measurements than conventional POCA approaches.

Elevation and elevation change models

We use a Lagrangian framework to derive elevation and rates of surface elevation change as to avoid interference of advecting ice-shelf topography [*Dutrieux et al.,* 2013; *Moholdt et al.,* 2014] (Figure S2). To this effect, we use ice velocity (supplementary section S3) to calculate and assign the position that each CryoSat-2 swath and POCA elevation measurements would have had at the beginning of the CryoSat-2 period, set at July 2010. The rates of surface elevation change and a Digital Elevation Model are then derived using a plane fit approach [*McMillan et al.,* 2014] applied to both the swath and POCA CryoSat-2 elevations. The map of rates of surface elevation change, $\dot{h}$, and the swath Digital Elevation Model, c_2, is solved on a grid of 500 m posting. We use a simple bi-linear model to describe the spatial variation of topography. We find that at 500 m resolution and over ice shelf a bi-linear model performs equally well, is more robust, and requires less computation power than a quadratic model:

$$z(x, y, t) = c_0 x + c_1 y + \dot{h} t + c_2 \quad (1)$$

where z are the CryoSat-2 elevation, and x, y, t are easting, northing and time respectively. For most cells, several hundreds of swath elevation measurements are present to constrain the model.

Error budget

We assign an uncertainty to the rate of surface elevation change of each individual pixel. Consider equation (1), the error $\varepsilon_{\dot{h}}$ on the rate of surface elevation change $\dot{h}$ is taken from the model covariance matrix cov m, calculated as:

$$\mathrm{cov\ m} = \mathrm{G}^{+}\ \mathrm{cov(z)}\ [\mathrm{G}^{+}]^{\mathrm{T}} \quad (2)$$

where the vector z are the input elevations, m = [c0 c1 $\dot{h}$ c2] represents the model parameters, G = [x y t 1] is the model matrix, $\boldsymbol{G}^{+}$ is its pseudo-inverse and $[\boldsymbol{G}^{+}]^{\mathrm{T}}$ is the transpose of the pseudo-inverse, and $\mathrm{cov(z)}$ the data covariance. The diagonal of $cov\ \mathrm{m}$ are the variances of the model parameters, therefore $\varepsilon_{\dot{h}}$ can be extracted as follows:

$$\varepsilon_{\dot{h}} = \sqrt{\mathrm{diag}(cov\ \mathrm{m})_3} \quad (3)$$

where $\mathrm{diag}()_3$ is the third element on the diagonal.

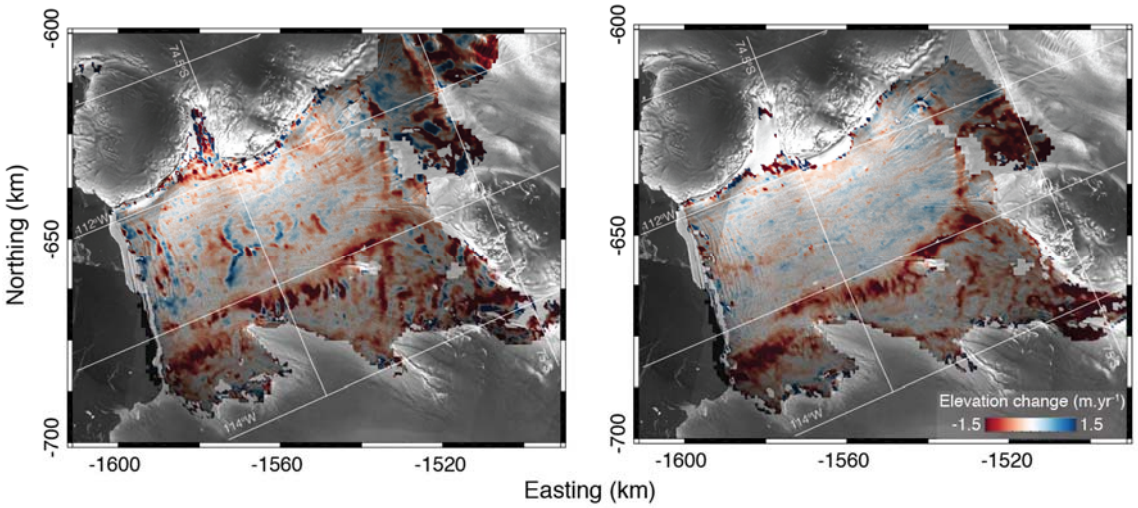

Figure S2: Rates of surface elevation change derived using an Eulerian (left) and Lagrangian (right) framework. Advection of surface topography in the Eulerian solution produces small-scale, transient, signal.

Comparison with Operation Ice Bridge's Airborne Topographic Mapper instrument

Comparison of the CryoSat-2 swath DEM with ATM elevation for the year 2010, corresponding to the timestamp of the CryoSat-2 Digital Elevation model, reveal an elevation bias and dispersion of -1.5±1.2 m, reflecting the penetration of Ku band signal into snow and firn as well as the effect of the difference in instrument footprint between ATM and CryoSat-2 leading to different sensitivity to small scale features such as surface crevasses (Figure S3). A -1.5 m bias is corrected from the CryoSat-2 elevation for the melt rate computation (Supplementary Section S3).

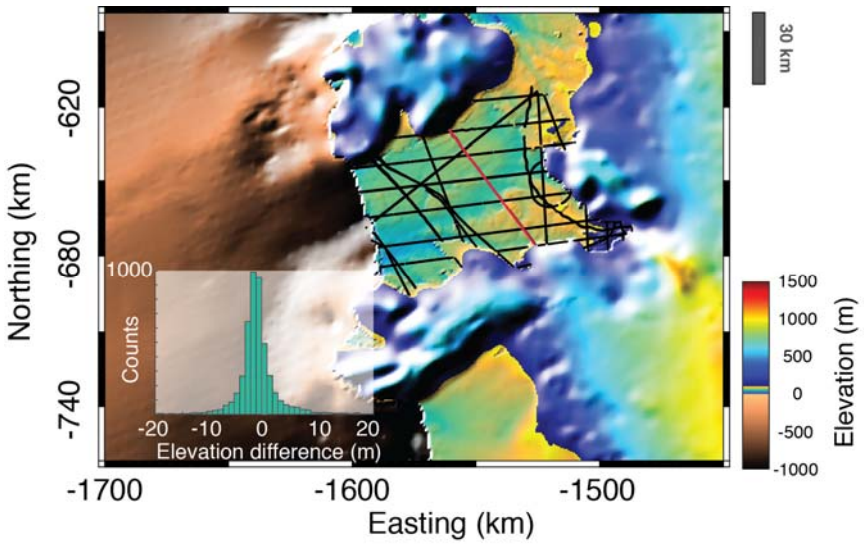

Figure S3: Bathymetry and topography in the Dotson Ice Shelf region. The topography of the ice sheet and ice shelves is from Bedmap2 [*Fretwell et al.,* 2013]**, with the exception of the topography of DIS obtained from CryoSat-2 swath altimetry; the bathymetry is from RTopo** [*Timmermann et al.,* 2010]**. Operation Ice Bridge ATM flights line (black lines). The flight line used in figure S4 is shown in red.**

72

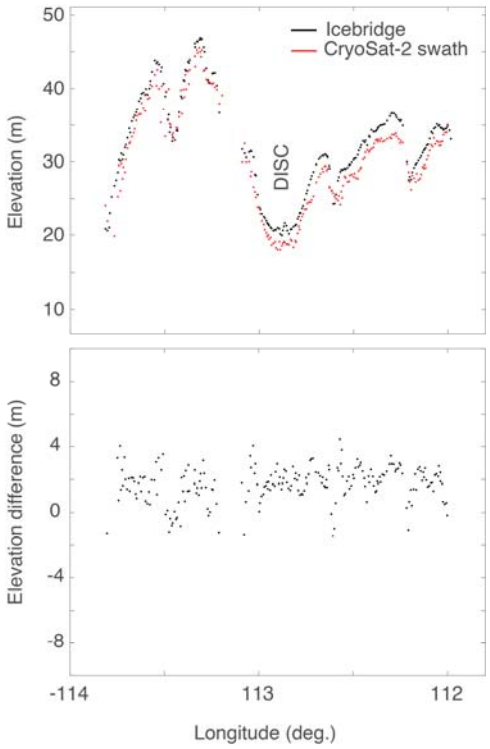

Figure S4: An example of elevation profile across the DISC from icebridge and CryoSat-2 swath showing that CryoSat recovers well the small-scale topographic features across the shelf. The location of the profile is shown in figure S3.

POCA vs Swath

We derived rates of surface elevation change determined from CryoSat-2's POCA elevation at 1 km posting (higher resolutions are unfeasible due to the insufficient data density). The results obtained with POCA show similar rates of elevation change patterns as the product obtained from Swath altimetry but with less spatial details; it also performs poorly at the margins of the ice shelf (Figure S5).

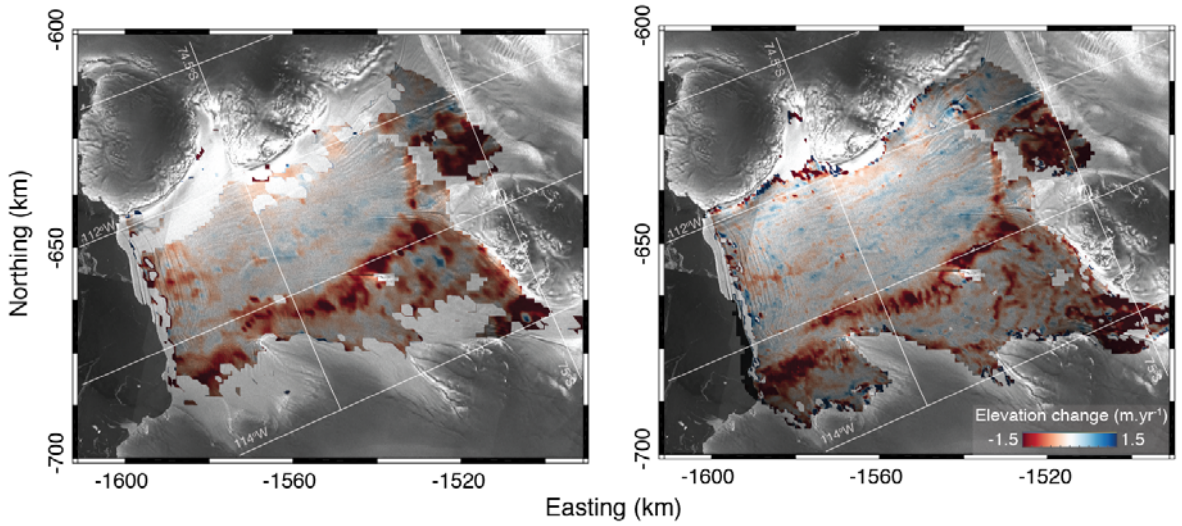

Figure S5: Rates of surface elevation change derived from POCA elevation (left) and Swath elevation (right).

80

81 **Rates of elevation change from 1991 to 2010 from low-resolution radar altimetry**

82 We used satellite radar altimetry data acquired between May 1991 and September 2010 to
83 generate a 21–year record of ice shelf thickness change on the Dotson Ice Shelf (Figure S6).
84 Level-2 elevation data from the European Remote Sensing (ERS) -1, -2, and ENVISAT
85 satellites was geophysically corrected using the wet atmosphere, dry atmosphere, ionosphere,
86 inverse barometric, solid earth and ocean loading tides. The auxiliary CATS2008a tide
87 correction was used to correct the satellite elevations for ocean tides [*Padman et al.,* 2002].
88 The satellite data were binned into a 2 km by 2 km grid, and a plane fit solution was used to
89 derive elevation change using time, slope-corrected geographic location, slope- and
90 geophysically-corrected height, backscatter power and orbit heading [*McMillan et al.,* 2014].
91 Outliers were removed if the measured height was > 2 standard deviations from the modelled
92 height, and the model fit was iterated until all remaining points met the deviation criterion or
93 less than 15 data points remained. Grid cells were discarded if they contained less than 15
94 data points after the iterative plane fit. The output data was masked to retain a solution over
95 the ice shelf area only, which was defined by the grounding line measured using differential
96 interferometry [*Rignot et al.,* 2014], and the calving front location [*Zwally et al.,* 2012]. Data

97 gaps in the output dh/dt grid were filled using an inverse distance filling algorithm with a 25 km
98 radius, and the final dataset was smoothed using a median filter with a 6 km (3 pixel) radius.

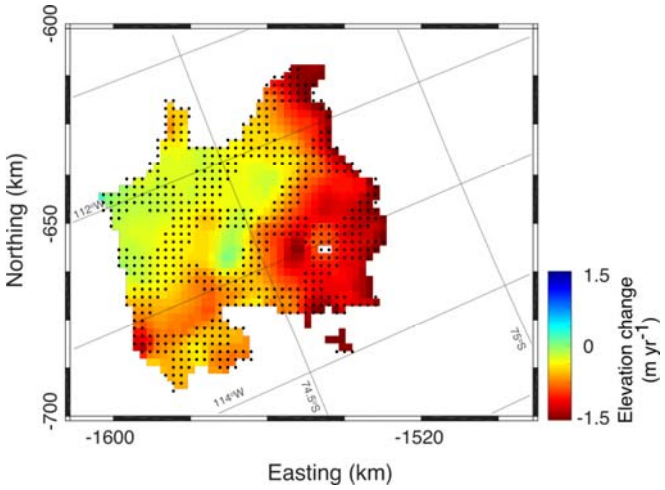

Figure S6: Mean rates of surface elevation change derived from ERS1/2 and Envisat for the period 1991-2010 and location of grid cells with valid measurements (black dots).

99

100

101 **S2. RADAR DATA**

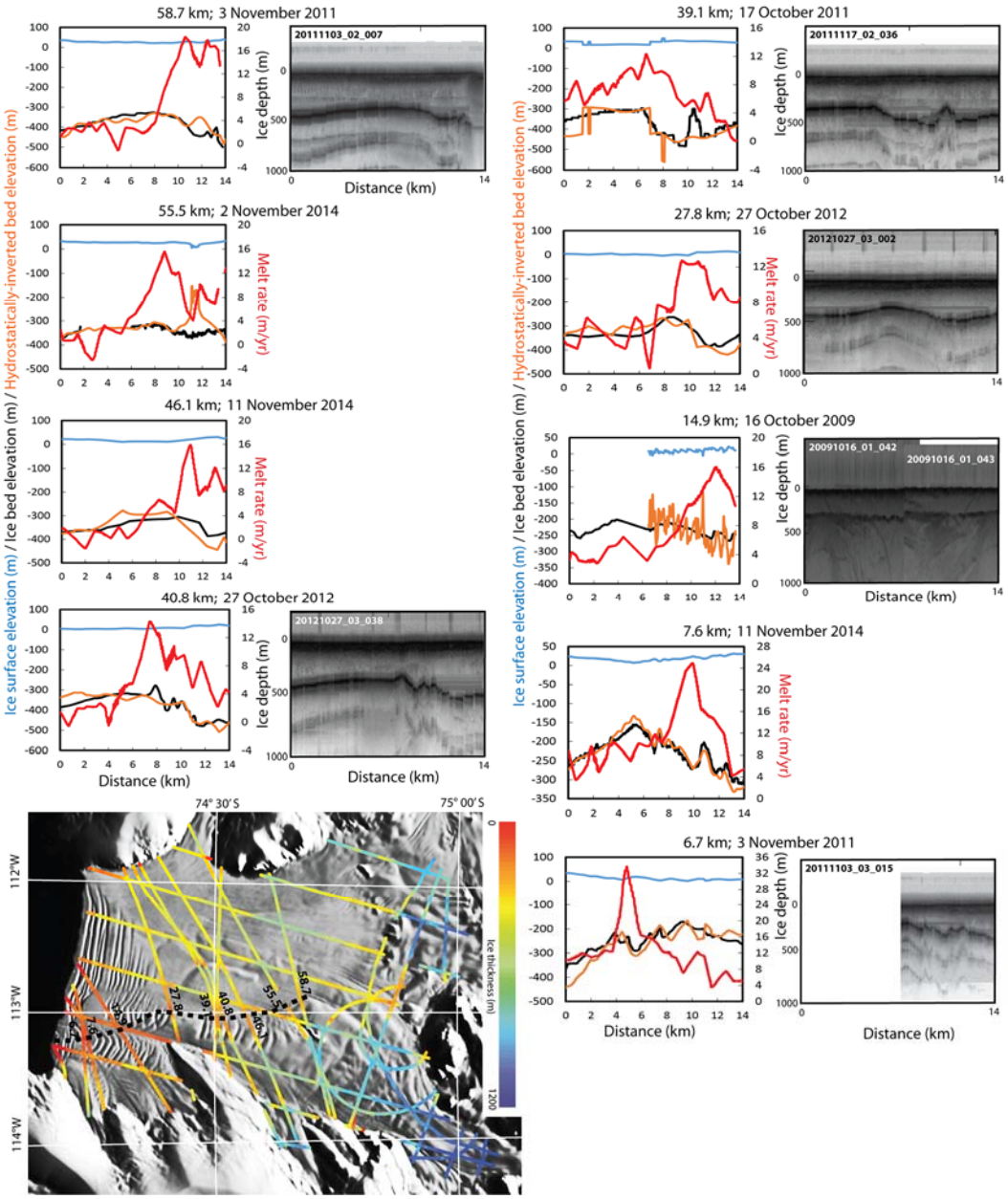

Figure S7: Radar-derived ice elevation and profiles across Dotson Ice Shelf Channel. Bottom-left panel shows ice surface and basal elevation picked from NASA Operation Ice Bridge tracks acquired from 2009 to 2014 as well as basal melt from this study. Black dotted line depicts axis of ice-shelf channel; the numbers state distance from the calving front and cross-reference to (all other panels) progressive cross-sections of ice-surface elevation (blue), ice-bed elevation (black), inverted hydrostatic ice-bed elevation (orange) and basal melt rate (red). Radargrams from the Operation Ice

Bridge online portal are also shown where available. Background to bottom-left panel from MODIS.

S3. EARTH-OBSERVATION DERIVED ICE SHELF BASAL MELTING

The melt rate of DIS is assessed through the following, modified from the main text and from [*Jenkins and Doake,* 1991]:

$$-\left(1-\frac{\rho_i}{\rho_w}\right)\dot{m}+SMB=\frac{\partial S}{dt}+S\nabla\cdot\mathbf{u} \tag{4}$$

where m is basal melt rate, ρ_i is ice density of 917 kg m^{-3}, ρ_w nominal ocean density of 1028 kg m^{-3}, $\mathbf{u}$ is velocity, S is surface elevation from the DEM, corrected for a 1.5 m penetration bias.

Equation (4) does not take account of firn thickness, which we justify here. We assume the ice shelf is incompressible, regardless of whether it is glacial ice or firn [*Ng and King,* 2011]. This means that vertical stretching and compression rate due to horizontal divergence and convergence is constant for a column. The equation for thickness evolution is given by

$$\frac{\partial h}{dt}=-\nabla\cdot(\mathbf{u}h)+SMB-\dot{m} \tag{5}$$

Meanwhile, if ε is the thickness of air in a column, then hydrostatic floatation implies

$$\rho_w b=\rho_i(h-\varepsilon) \tag{6}$$

where b is thickness below sea level. Since $h = S + b$,

$$h=\left(1-\frac{\rho_i}{\rho_w}\right)^{-1}\left(s-\frac{\rho_i}{\rho_w}\varepsilon\right) \tag{7}$$

Replacing h with (7) in (5) yields

$$\left(1-\frac{\rho_i}{\rho_w}\right)^{-1}\left(\frac{\partial S}{dt}+\nabla\cdot(\mathbf{u}S)-\frac{\rho_i}{\rho_w}\left[\frac{\partial \varepsilon}{dt}+\nabla\cdot(\mathbf{u}\varepsilon)\right]\right)=SMB-\dot{m}. \quad (8)$$

118

119 Assuming there is no air in basal ice, basal melting will not affect ε, thus the term

$$\frac{\partial \varepsilon}{dt}+\nabla\cdot(\mathbf{u}\varepsilon) \quad (9)$$

120 i.e. the net rate input of air, is due only to surface processes. Figure S8 indicates this value is
121 small (less than 5 cm/year over most of DIS), and so we neglect it, yielding (4).

122 **Surface Mass Balance**

123 Surface Mass Balance (SMB) is obtained from output of the regional atmospheric climate
124 model RACMO, version 2 (RACMO2 hereafter). In this most recent version, the model
125 includes new cloud and drifting snow physics, which further improve its representation of
126 Antarctic SMB [*Lenaerts et al.,* 2012; *Van Wessem et al.,* 2014; *van, Wessem et al.,* 2016]. At
127 the lateral and sea-ice/ocean surface boundaries, the model is forced by ERA-Interim
128 reanalyses (1979-present). RACMO2 uses a spatial domain centred on the Amundsen Sea
129 coast, and has a horizontal resolution of approximately 5.5 km. In summary, the 5.5 km
130 simulation compares better with 2m temperature and 10m wind speed observations from 9
131 automatic weather station than the 27 km simulation (r^2 score for 3-hourly measurements is
132 17-1 for 5.5 km vs. 27 km). The spatial patterns in accumulation and melt show obviously more
133 detail and compare on average better with accumulation radar observations [*Medley et al.,*
134 2013] and satellite observed melt extent [*Trusel et al.,* 2013]. We note here that there are
135 suggestions of SMB variation across channels that would not be represented by the 5.5 km
136 simulation [*Langley et al.,* 2014; *Drews,* 2015]; however these variations are hypothesised for
137 channels much smaller than the one observed here.

138 **Firn layer processes**

The observed rates of surface elevation change can be caused by multiple processes, which we divide here in two regimes: 1) changes at the surface and within the firn column and 2) changes in the ice column or at the ice-ocean interface. To obtain the former, we use the firn densification model IMAU-FDM [*Ligtenberg et al.,* 2011] to simulate all processes at the surface and in the firn column. IMAU-FDM is a 1-D column model that calculates the total surface elevation change caused by surface mass accumulation/loss, dry firn compaction, and surface melt water processes (percolation, refreezing, retention, and runoff). The model does not take ice advection into account, but this is deemed reasonable as 1) only simulated surface elevation changes over relative short time periods (< 10 years) are considered, and 2) longitudinal stresses do not affect elevation changes due to SMB processes. At the surface, it is forced by 3-hourly climate output from the regional climate model RACMO2, such as surface temperature, wind speed, precipitation (solid and liquid), sublimation, drifting snow erosion/deposition, and surface melt. On ice shelves, IMAU-FDM also corrects the surface elevation signal for the buoyancy effect of a higher/lower SMB. Figure S8 shows the resulting surface elevation change between 2010 and 2016, which on average is very small: 0.4 mm yr^{-1}. However, locally it can be in the order of 5-10 cm yr^{-1}.

Along with surface elevation changes, IMAU-FDM also simulates the evolution of firn density and temperature with depth. The first is used here to distinguish between the amount of air and ice in the firn column. The firn air content is calculated as the vertically integrated difference between the simulated density and the density of glacier ice (917 kg m^{-3}) and given in meters. By subtracting the firn air content from the observed surface elevation, the ice-equivalent thickness of the ice shelf is calculated using the floatation criterion with the density of ice and ocean water.

Firn density variation may be occurring across channels [*Drews et al.,* 2016] and are not represented in the model; if this density variation was confirmed this would have a small impact on the height of the sub-shelf channels derived from surface elevation.

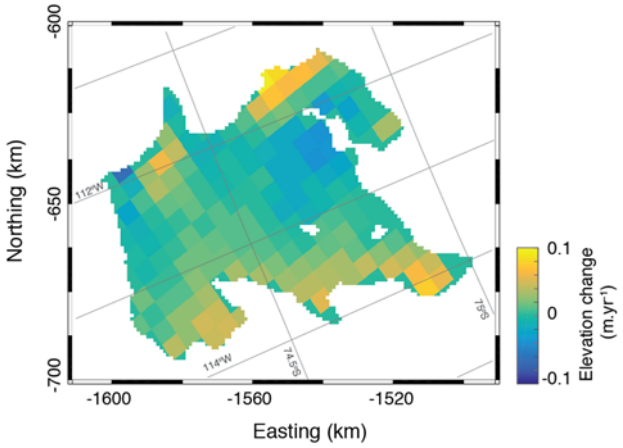

Figure S8: Rates of surface elevation change between 2010 and 2016 due to firn processes. Mean rate of elevation change for DIS is 4.10^{-4} m yr^{-1}.

Ice velocities

Velocity for the 2008 period are from MEaSUREs [*Mouginot et al.,* 2012]. The recent mosaic of ice surface velocity is derived from a series of satellite SAR images acquired by Sentinel-1a/ESA between December 2014 and June 2016, and optical images acquired by Landsat/USGS between July 2013 and June 2016. SAR offsets between image pairs is derived from the speckle tracking method and converted to ice surface displacement assuming surface parallel flow. Optical offsets are derived using standard cross-correlation methods [*Dehecq et al.,* 2015]. The resulting offsets were filtered, calibrated and combined in single annual averaged mosaics [*Mouginot et al.,* 2012; *McMillan et al.,* 2012]. The averaging is done by attributing different weights for each velocity estimate based on the spatial resolution and time interval between the two acquisitions. We estimate the errors to be around 40 m yr^{-1} for the Dotson Ice Shelf. This process generates the direction and magnitude of the ice velocity which are then used to calculated Lagrangian rates of elevation changes, as well as advection and dynamic thinning.

Advection and dynamic thinning

Advection and dynamic thinning (the second and third terms on the right hand side of equation (4), respectively) are calculated using the CryoSat DEM, along with satellite-derived velocities. Velocities are interpolated to a C-grid [*Arakawa and Lamb,* 1977], on which elevations reside

at cell centers. Flux of elevation (u_xS, u_yS) is then calculated in an upwinded fashion. The dynamic thinning term is calculated with a baseline of 5km.

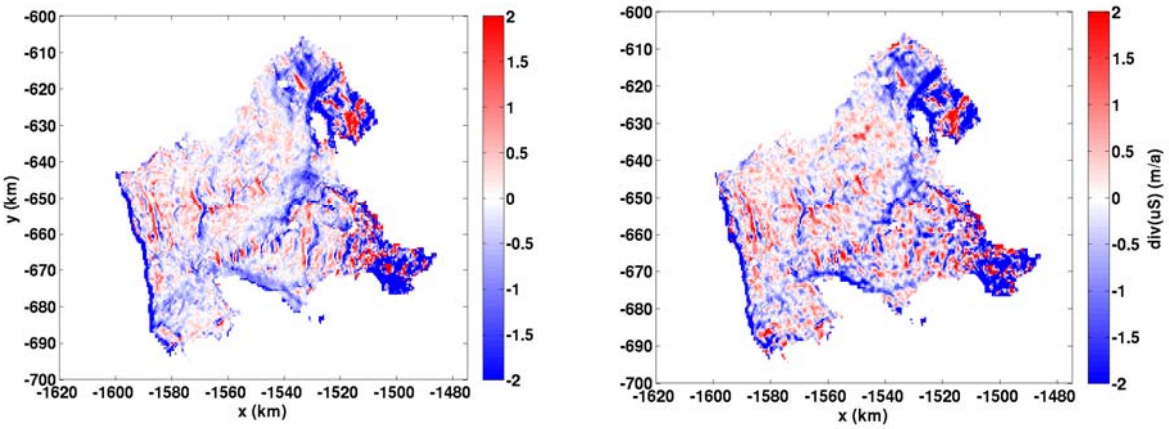

Figure S9: Sum of advective and diffusive term for DIS using MEaSUREs (left) and more recent (right) velocities.

The sum of the advective and dynamic thinning terms are shown in Figure S9 for the two different velocity datasets. Note that surface elevation is identical for the two products. The patterns are similar, although the MEaSUREs product shows less noise. Strong convergence, likely a response to melt-induced thinning, is seen near the shelf front along the western margin. Strong convergence also occurs near the outlet of Kohler Glacier in the southwest of the shelf, which is not visible in the observed thinning pattern, indicating high melt rates to balance the ice input.

Uncertainties

The uncertainty on melt rate is obtained from linear propagation of the SMB, divergence and advection, and surface elevation change errors and is given in the main manuscript.

REFERENCES

Arakawa, A. and V. R. Lamb (1977), Computational design of the basic dynamical processes of the UCLA general circulation model, in *Methods in Computational Physics: Advances in Research and Applications*, vol. 17, edited by J. CHANG, pp. 173-265, Elsevier.

Dehecq, A., N. Gourmelen, and E. Trouve (2015), Deriving large-scale glacier velocities from a complete satellite archive: Application to the Pamir–Karakoram–Himalaya*, Remote Sens. Environ., 162*, 55-66.

Drews, R. (2015), Evolution of ice-shelf channels in Antarctic ice shelves*, The Cryosphere, 9*, 1169-1181.

Drews, R., J. Brown, K. Matsuoka, E. Witrant, M. Philippe, B. Hubbard, and F. Pattyn (2016), Constraining variable density of ice shelves using wide-angle radar~measurements*, The Cryosphere, 10*, 811-823.

Dutrieux, P., D. G. Vaughan, H. F. J. Corr, A. Jenkins, P. R. Holland, I. Joughin, and A. H. Fleming (2013), Pine Island glacier ice shelf melt distributed at kilometre scales*, The Cryosphere, 7*, 1543-1555.

Foresta, L., N. Gourmelen, F. Pálsson, P. Nienow, H. Björnsson, and A. Shepherd (2016), Surface elevation change and mass balance of Icelandic ice caps derived from swath mode CryoSat-2 altimetry*, Geophys. Res. Lett., 43*, 12,138-12,145.

Fretwell, P. et al. (2013), Bedmap2: improved ice bed, surface and thickness datasets for Antarctica*, The Cryosphere, 7*, 375-393.

Gray, L., D. Burgess, L. Copland, R. Cullen, N. Galin, R. Hawley, and V. Helm (2013), Interferometric swath processing of Cryosat-2 data for glacial ice topography*, The Cryosphere Discussions, 7*, 3133-3162.

225 Hawley, R. L., A. Shepherd, R. Cullen, V. Helm, and D. J. Wingham (2009), Ice-sheet
226 elevations from across-track processing of airborne interferometric radar altimetry, *Geophys.*
227 *Res. Lett., 36*.

228 Jenkins, A. and C. S. M. Doake (1991), Ice-Ocean Interaction on Ronne Ice Shelf,
229 Antarctica, *J. Geophys. Res., 96*, 791-813.

230 Langley, K., A. von Deschwanden, J. Kohler, A. Sinisalo, K. Matsuoka, T. Hattermann, A.
231 Humbert, O. A. Nøst, and E. Isaksson (2014), Complex network of channels beneath an
232 Antarctic ice shelf, *Geophys. Res. Lett., 41*, 1209-1215.

233 Lenaerts, J. T. M., M. R. van den Broeke, W. J. van de Berg, E. van Meijgaard, and P.
234 Kuipers Munneke (2012), A new, high-resolution surface mass balance map of Antarctica
235 (1979–2010) based on regional atmospheric climate modeling, *Geophys. Res. Lett., 39*.

236 Ligtenberg, S. R. M., M. M. Helsen, and M. R. van den Broeke (2011), An improved semi-
237 empirical model for the densification of Antarctic firn, *The Cryosphere, 5*, 809-819.

238 McMillan, M., Shepherd A., N. Gourmelen, J. W. Park, P. Nienow, E. Rinne, and A. Leeson
239 (2012), Mapping ice-shelf flow with interferometric synthetic aperture radar stacking, *Journal*
240 *of Glaciology, 58*, 265-277.

241 McMillan, M., A. Shepherd, P. Nienow, and A. Leeson (2011), Tide model accuracy in the
242 Amundsen Sea, Antarctica, from radar interferometry observations of ice shelf motion,
243 *Journal of Geophysical Research: Oceans, 116*.

244 McMillan, M., A. Shepherd, A. Sundal, K. Briggs, A. Muir, A. Ridout, A. Hogg, and D.
245 Wingham (2014), Increased ice losses from Antarctica detected by CryoSat-2, *Geophys.*
246 *Res. Lett., 41*, 3899-3905.

247 Medley, B. et al. (2013), Airborne-radar and ice-core observations of annual snow
248 accumulation over Thwaites Glacier, West Antarctica confirm the spatiotemporal variability of
249 global and regional atmospheric models, *Geophys. Res. Lett., 40*, 3649-3654.

250 Moholdt, G., L. Padman, and H. A. Fricker (2014), Basal mass budget of Ross and Filchner-
251 Ronne ice shelves, Antarctica, derived from Lagrangian analysis of ICESat altimetry, *Journal*
252 *of Geophysical Research: Earth Surface, 119*, 2361-2380.

253 Mouginot, J., B. Scheuchl, and E. Rignot (2012), Mapping of Ice Motion in Antarctica Using
254 Synthetic-Aperture Radar Data, *Remote Sensing, 4*, 2753.

255 Ng, F. and E. C. King (2011), Kinematic waves in polar firn stratigraphy, *J. Glaciol., 57*,
256 1119-1134.

257 Padman, L., H. A. Fricker, R. Coleman, S. Howard, and L. Erofeeva (2002), A new tide
258 model for the Antarctic ice shelves and seas, *Annals of Glaciology, Vol 34, 2002, 34*, 247-
259 254.

260 Rignot, E., J. Mouginot, M. Morlighem, H. Seroussi, and B. Scheuchl (2014), Widespread,
261 rapid grounding line retreat of Pine Island, Thwaites, Smith, and Kohler glaciers, West
262 Antarctica, from 1992 to 2011, *Geophys. Res. Lett., 41*, 3502-3509.

263 Timmermann, R. et al. (2010), Antarctic ice sheet topography, cavity geometry, and global
264 bathymetry (RTopo 1.0.5-beta), *Supplement to: Timmermann, R et al.(2010): A consistent*
265 *dataset of Antarctic ice sheet topography, cavity geometry, and global bathymetry.Earth*
266 *System Science Data, 2(2), 261-273, doi:10.5194/essd-2-261-2010*.

267 Trusel, L. D., K. E. Frey, S. B. Das, P. K. Munneke, and M. R. van den Broeke (2013),
268 Satellite-based estimates of Antarctic surface meltwater fluxes, *Geophys. Res. Lett., 40*,
269 6148-6153.

Van Wessem, J. M. et al. (2014), Improved representation of East Antarctic surface mass balance in a regional atmospheric climate model*, J. Glaciol., 60*, 761-770.

van, Wessem, J. M. et al. (2016), The modelled surface mass balance of the Antarctic Peninsula at 5.5 km horizontal resolution*, The Cryosphere, 10*, 271-285.

Zwally, H. J., M. B. Giovinetto, M. A. Beckley, and J. L. Saba (2012), Antarctic and Greenland Drainage Systems, *GSFC Cryospheric Sciences Laboratory*.